

A dynamical approach in exploring the unknown mass in the Solar system using pulsar timing arrays

Y. J. Guo¹, K. J. Lee^{1,2*} and R. N. Caballero³

¹*Kavli Institute for Astronomy and Astrophysics, Peking University, Beijing 100871, People's Republic of China*

²*National Astronomical Observatories, Chinese Academy of Sciences, Beijing 100012, China*

³*Max-Planck-Institut für Radioastronomie, Auf Dem Hügel 69, Bonn 53121, Deutschland*

Accepted XXX. Received YYY; in original form ZZZ

ABSTRACT

The error in the Solar system ephemeris will lead to dipolar correlations in the residuals of pulsar timing array for widely separated pulsars. In this paper, we utilize such correlated signals, and construct a Bayesian data-analysis framework to detect the unknown mass in the Solar system and to measure the orbital parameters. The algorithm is designed to calculate the waveform of the induced pulsar-timing residuals due to the unmodelled objects following the Keplerian orbits in the Solar system. The algorithm incorporates a Bayesian-analysis suit used to simultaneously analyse the pulsar-timing data of multiple pulsars to search for coherent waveforms, evaluate the detection significance of unknown objects, and to measure their parameters. When the object is not detectable, our algorithm can be used to place upper limits on the mass. The algorithm is verified using simulated data sets, and cross-checked with analytical calculations. We also investigate the capability of future pulsar-timing-array experiments in detecting the unknown objects. We expect that the future pulsar timing data can limit the unknown massive objects in the Solar system to be lighter than 10^{-11} to $10^{-12} M_{\odot}$, or measure the mass of Jovian system to fractional precision of 10^{-8} to 10^{-9} .

Key words: pulsar:general – minor planets, asteroids: general – methods: data analysis

1 INTRODUCTION

The clock-like rotational stability of millisecond pulsars makes them the the most accurate celestial clocks known. Through the process of pulsar timing (e.g. Lorimer & Kramer 2005; Hobbs et al. 2006), millisecond pulsars are powerful tools for a wide range of scientific problems. In the process of pulsar timing, the time of arrivals (TOAs) recorded at the observatory are transferred to the pulsar frame. The differences between the observed TOAs and the model predictions form the timing residuals. The physical processes not modelled will leave their fingerprints in the timing residuals. For processes affecting all the pulsars, they introduce the correlated signals between widely separated pulsar pairs. Such spatial correlations have profound applications. For example, one can detect the gravitational waves (GW; Hellings & Downs 1983), investigate the stability of reference terrestrial time standards (Hobbs et al. 2012), and study the Solar system ephemeris (Champion et al. 2010). These applications make use of so-called pulsar timing ar-

rays (PTAs), which are an ensemble of pulsars, typically millisecond pulsars, in different sky positions (Foster & Backer 1990).

The first step in converting the site TOAs to the pulse-emission time at the pulsar frame, is to refer them to the Solar system barycentre (SSB) according to the SSB position with respect to the Earth. In the common pulsar timing practice, the SSB position is provided by the Solar system ephemeris (Standish 1998). Errors in the used ephemeris will then lead to inaccurate conversion of TOAs, and thus induce the correlated timing residuals among all analysed pulsars. We can study the Solar system ephemeris by searching for such correlated residuals.

Champion et al. (2010) were the first to employ a PTA to constrain the mass of planets in the Solar system . They fixed the orbits of the known planets using the DE421 ephemeris (Folkner et al. 2009) and investigated the effects of perturbing the input planetary masses on the TOAs. In this way, they used the PTA data to constrain possible errors in the Solar system ephemeris, and provide upper limits on the masses of planets (or planetary systems when satellites are in orbit).

* E-mail: kjlee@pku.edu.cn

Possible errors in the Solar system ephemeris may come from two aspects: inaccurate mass or position of known objects, and the existence of unmodelled objects (UMOs). Champion et al. (2010) had studied the error in the mass of known planets. In this paper, we want to explore the unknown objects in the Solar system by pulsar timing, to detect their signal or put upper limits on their masses. The term UMOs here refers to any unknown objects revolving around the SSB, such as dark matter clumps (Loeb & Zaldarriaga 2005; Pitjev & Pitjeva 2013), small asteroids (Sheppard & Trujillo 2016), strangelets (Wu et al. 2007), cosmic strings (Blanco-Pillado et al. 2014), tiny primordial black holes or other unidentified massive objects. The studies of timing residuals induced by the ephemeris can help us understand the noise budget of PTAs, which is of central importance for the GW detection with PTAs. Furthermore, a better Solar system ephemeris may also improve the precision of deep space missions.

In the current paper, we model the UMOs with Keplerian orbits, calculate the induced timing residuals, and perform parameter estimation using Bayesian inference. We describe our methods in Section 2, and use simulations to verify our algorithm in Section 3. We analytically calculate the PTA sensitivity to the UMOs and investigate the capability of future PTA experiments in Section 4. Discussions and conclusions are made in Section 5.

2 METHODS

We use a model-based Bayesian data-analysis method to measure the mass of UMOs using PTA data. There are two major components for the Bayesian inference, the signal model (in Section 2.1) and the likelihood model (in Section 2.2).

2.1 Pulsar-timing residuals induced by UMOs

Pulsar timing residuals \mathbf{R} can be described as the sum of three sources: the signal $\Delta\mathbf{R}$, induced by unmodelled processes such as the orbit of a UMO, the signal \mathbf{s} , induced by imperfectly modelled timing parameters, and the signal \mathbf{n} , from noise processes. That is

$$\mathbf{R} = \Delta\mathbf{R} + \mathbf{s} + \mathbf{n}. \quad (1)$$

In most of the pulsar-timing procedures, one uses the clock corrections published by the Bureau International des Poids et Mesures (BIPM)¹, Earth orientation parameters and Solar system ephemeris to correct the TOAs seen at the telescope site to the TOAs as seen in the pulsar rest frame. In this way, any objects not included in the ephemeris will introduce signals in the pulsar timing residuals. Such signals have a dipolar spatial correlation, different from the monopolar correlation induced by clock errors (Hobbs et al. 2012). In this paper, we focus on the leading-order effects of the UMOs under the following two assumptions.

(i) We assume that the UMO follows a point-mass Keplerian orbit around the SSB. In particular, we focus on

bound systems, of which orbits are elliptic. The major acceleration of the UMO is thus due to the Sun, and we neglect the higher-order effects, such as the perturbations from objects except the Sun in the Solar system, the post-Newtonian corrections, and tidal forces.

(ii) The UMOs induce periodic motion of the SSB. Such motion will contribute to the pulsar-Earth distance and lead to an extra geometric time delay in the pulsar TOAs (i.e. the Rømer delay as explained in Edwards et al. (2006)). We have neglected the higher-order effects due to the SSB motion (e.g. parallax, gravitational redshifts, and Shapiro delay), as done by Champion et al. (2010).

Champion et al. (2010) showed that the perturbation of Jupiter mass simply changes the position of the SSB, as we modelled. It is unclear if such perturbative approach is also valid for the other planets, especially the ones with inner orbits. Investigating the long-term evolution of the Solar system dynamics with full modelling is beyond the scope of this article. However, the data length is limited to only a couple of tens of years, such that the first-order treatment, i.e. UMOs induce SSB shifts, is a valid approximation.

The Rømer delay ΔR associated with the displacement \mathbf{d}_s of the SSB is

$$\Delta R = -\frac{\mathbf{d}_s \cdot \mathbf{p}}{c}, \quad (2)$$

where \mathbf{p} is the unit vector pointing to the direction of the pulsar, and c is the speed of light. As we neglected the interaction between UMO and other Solar system objects other than the Sun, the displacement of the SSB caused by the UMO with mass $m \ll M_\odot$ and position vector \mathbf{r} relative to the original SSB is

$$\mathbf{d}_s = \frac{m}{M} \mathbf{r}, \quad (3)$$

where M is the total mass of the Solar system and can be well approximated by the solar mass, such that $M \simeq M_\odot$.

The Keplerian orbit of a UMO is modelled with seven parameters ($\xi_i, i = 1 \dots 7$), which fully determine the induced pulsar-timing residuals. The ξ parameters contain the mass of the UMO and six orbital elements. The orbital elements determine the geometry of orbit, and are the semi-major axis, a , eccentricity, e , longitude of the ascending node, Ω , orbital inclination angle, i , argument of perihelion ω , and phase at reference epoch, φ_0 .

For elliptic orbits, the radial distance of a UMO to the centre of mass, r , can be expressed in terms of the eccentric anomaly, u , as

$$r = a(1 - e \cos u). \quad (4)$$

The evolution of u with time t satisfies

$$u - e \sin u = 2\pi ft - \varphi_0, \quad (5)$$

where f is the orbital frequency. The latter follows Kepler's third law, such that

$$f = \frac{1}{2\pi} \sqrt{\frac{GM}{a^3}}. \quad (6)$$

Using the true anomaly ν , the position vector \mathbf{r}_0 of the UMO in the orbital plane becomes

$$\mathbf{r}_0 = \begin{pmatrix} r \cos \nu \\ r \sin \nu \\ 0 \end{pmatrix}, \quad (7)$$

¹ <http://www.bipm.org/>

and the true anomaly is defined as

$$\nu = 2 \arctan \left[\sqrt{\frac{1+e}{1-e}} \tan \left(\frac{u}{2} \right) \right]. \quad (8)$$

We transform the position vector to the ecliptic coordinate using rotation matrix as computed from the Euler angles of orbital elements, such that

$$\mathbf{r} = \mathbf{R}_z(-\Omega) \mathbf{R}_x(-\iota) \mathbf{R}_z(-\omega) \mathbf{r}_0, \quad (9)$$

$$\mathbf{R}_z(-\Omega) = \begin{pmatrix} \cos \Omega & -\sin \Omega & 0 \\ \sin \Omega & \cos \Omega & 0 \\ 0 & 0 & 1 \end{pmatrix}, \quad (10)$$

$$\mathbf{R}_x(-\iota) = \begin{pmatrix} 1 & 0 & 0 \\ 0 & \cos \iota & -\sin \iota \\ 0 & \sin \iota & \cos \iota \end{pmatrix}. \quad (11)$$

The dependence of the timing residuals, s , on the timing parameters, $\boldsymbol{\lambda}$, is usually non-linear, but the timing model can be linearized around the reference timing parameters, $\boldsymbol{\lambda}_0$, to compute the timing residuals (Manchester & Taylor 1977; Lorimer & Kramer 2005; Edwards et al. 2006; van Haasteren et al. 2009), which leads to

$$s_i = \sum_k D_{ik} (\lambda_k - \lambda_{0,k}) = \sum_k D_{ik} \delta \lambda_k. \quad (12)$$

Here, i is the index of each epoch of observation, and k is an index for the timing parameter. \mathbf{D} is the design matrix (the coefficients of linearization), and $\delta \boldsymbol{\lambda}$ is the deviation of timing parameters from the reference values.

Unlike the deterministic signal ΔR and s , the noise components, n , in the timing residuals are random. We model them through the likelihood function as described in the next section.

2.2 The likelihood function and Bayesian inference

We perform the parameter estimation using Bayesian inference. The Bayesian techniques had been studied extensively in the field of pulsar timing (van Haasteren et al. 2009; Lee et al. 2014; Caballero et al. 2016; Lentati et al. 2016). Bayesian inference relies on converting the ‘probability of data’ to the ‘probability of parameters’ using Bayes’ theorem,

$$P(\boldsymbol{\zeta}|\mathbf{X}) = \frac{P(\boldsymbol{\zeta})P(\mathbf{X}|\boldsymbol{\zeta})}{P(\mathbf{X})}, \quad (13)$$

where \mathbf{X} is the data, and $\boldsymbol{\zeta}$ are the parameters to be inferred. $P(\mathbf{X}|\boldsymbol{\zeta}) \equiv \Lambda$ is the likelihood function, i.e. the probability density function for the data given the parameters. $P(\boldsymbol{\zeta}|\mathbf{X})$ is the posterior probability distribution, i.e. the probability density function for the parameters given the data set. The Bayesian evidence $P(\mathbf{X})$ is a normalization coefficient, defined as

$$P(\mathbf{X}) = \int P(\boldsymbol{\zeta})P(\mathbf{X}|\boldsymbol{\zeta})d\boldsymbol{\zeta}. \quad (14)$$

The prior probability distribution $P(\boldsymbol{\zeta})$ describes *a priori* belief about the distribution of the model’s parameters.

In the current paper, we assume the random noise in pulsar-timing residual of individual pulsars is a zero-mean Gaussian process. This approach had been taken by many

authors. We refer the interested readers to Lee et al. (2014) or Caballero et al. (2016) for the details of single-pulsar noise modelling. Here we only briefly outline the definitions.

Under the Gaussian assumption the noise components \mathbf{n} can be fully characterized using the covariance matrix, \mathbf{C} ,

$$P(\mathbf{n}|\boldsymbol{\Theta}) = \frac{1}{\sqrt{(2\pi)^N |\mathbf{C}|}} \exp \left[-\frac{1}{2} \mathbf{n}^\top \mathbf{C}^{-1} \mathbf{n} \right], \quad (15)$$

where N is the number of data points, $\boldsymbol{\Theta}$ refers to the noise model parameters, and symbols $\|\|$, $^{-1}$, and $^\top$ are the determinant, inversion, and transpose operation for matrices, respectively.

The noise processes in pulsar timing, are usually classified into three major parts, white-noise, red-noise, and the frequency-dependent-noise processes (see Cordes 2013, for a review). In this paper, we focus on the first two, the white noise and red noise. The noise power is additive, if the white noise and red noise are uncorrelated. The noise covariance matrix becomes $\mathbf{C} = \mathbf{C}_w + \mathbf{C}_r$.

The white noise is modelled as the TOA uncertainty σ_i scaled by a systematic factor (‘Efac’), with σ_i determined by the template fitting of pulse profile (Hotan et al. 2004). We also include a possible independent source of white noise (such as jitter) which is modelled by Equad. The white noise covariance matrix becomes

$$C_{w,ij} = \begin{cases} \text{Efac}^2 \sigma_i^2 + \text{Equad}^2, & \text{if } i = j; \\ 0, & \text{if } i \neq j. \end{cases} \quad (16)$$

The red noise is modelled as a wide-sense stationary Gaussian stochastic signal with a power-law spectrum (Lee et al. 2014),

$$S_r(f) = \begin{cases} \frac{A_r^2}{f} \left(\frac{f}{f_c} \right)^{2\alpha_r}, & \text{if } f > 1/T; \\ 0, & \text{if } f < 1/T. \end{cases} \quad (17)$$

where $f_c = 1 \text{ yr}^{-1}$ is a reference frequency, and T is the data length. The Fourier transform of the spectral density gives the temporal correlation of the red noise,

$$C_{r,ij} = \int_{1/T}^{\infty} S_r(f) \cos(2\pi f t_{ij}) df, \quad (18)$$

where t_{ij} is the time difference between the i -th and j -th epoch.

With all the ingredients, the likelihood function for the UMO problem is

$$\begin{aligned} \Lambda &\equiv P(\mathbf{R}|\boldsymbol{\xi}, \delta \boldsymbol{\lambda}, \boldsymbol{\Theta}) \\ &= \frac{1}{\sqrt{(2\pi)^N |\mathbf{C}|}} e^{-\frac{1}{2} (\mathbf{R} - \boldsymbol{\Delta} \mathbf{R} - \mathbf{D} \delta \boldsymbol{\lambda})^\top \mathbf{C}^{-1} (\mathbf{R} - \boldsymbol{\Delta} \mathbf{R} - \mathbf{D} \delta \boldsymbol{\lambda})}. \end{aligned} \quad (19)$$

The parameters that we are interested in are the orbital elements $\boldsymbol{\xi}$. We can marginalise the likelihood function over the other parameters, which are referred to as ‘nuisance parameters’. The timing model parameters $\delta \boldsymbol{\lambda}$ are linear, and they can be marginalised analytically (van Haasteren et al. 2009) giving

$$P(\mathbf{R}|\boldsymbol{\xi}, \boldsymbol{\Theta}) = \sqrt{\frac{|\mathbf{C}'^{-1}| (2\pi)^M}{|\mathbf{C}| (2\pi)^N}} \exp \left[-\frac{\chi'^2}{2} \right], \quad (20)$$

Table 1. The pulsars used in the simulation and the values of the injected noise parameters (timing precision σ , amplitude A_r and spectral index α_r of the red noise).

PSR	$\sigma(\mu\text{s})$	$A_r(\mu\text{s})$	α_r
J0437–4715	0.3	0.08	-0.41
J1012+5307	1.7	0.20	-0.21
J1713+0747	0.3	0.09	-0.40
J1909–3744	0.2	0.02	-0.11
J2145–0750	1.2	0.31	-0.02

with

$$\mathbf{C}' = \mathbf{D}^T \mathbf{C}^{-1} \mathbf{D}, \quad (21)$$

$$\chi'^2 = (\mathbf{R} - \Delta \mathbf{R})^T (\mathbf{C}^{-1} - \mathbf{G})(\mathbf{R} - \Delta \mathbf{R}), \quad (22)$$

$$\mathbf{G} = \mathbf{C}^{-1} \mathbf{D} \mathbf{C}'^{-1} \mathbf{D}^T \mathbf{C}^{-1}, \quad (23)$$

where M is the number of timing model parameters.

The noise parameters in Θ are nonlinear, and their marginalisation can only be performed numerically. We marginalise them in the stage of stochastic sampling of the posterior. In this way, we fit the orbital elements and noise parameters simultaneously, with the parameters of timing model marginalised analytically.

Besides the likelihood function, the Bayesian analysis also depends on the prior distribution $P(\Theta)$. For the parameter estimation, one should use the least informative prior, the Jeffreys prior (Gregory 2005). The prior distributions are uniform for dimensionless parameters, while uniform in the log-space for the parameter with dimension. However, the logarithmic prior introduces an infinite-volume parameter space close to the origins, which makes the confidence level of upper limits invalid. As a consequence, the use of uniform priors is required to place reasonable upper limits (Caballero et al. 2016; Lentati et al. 2016).

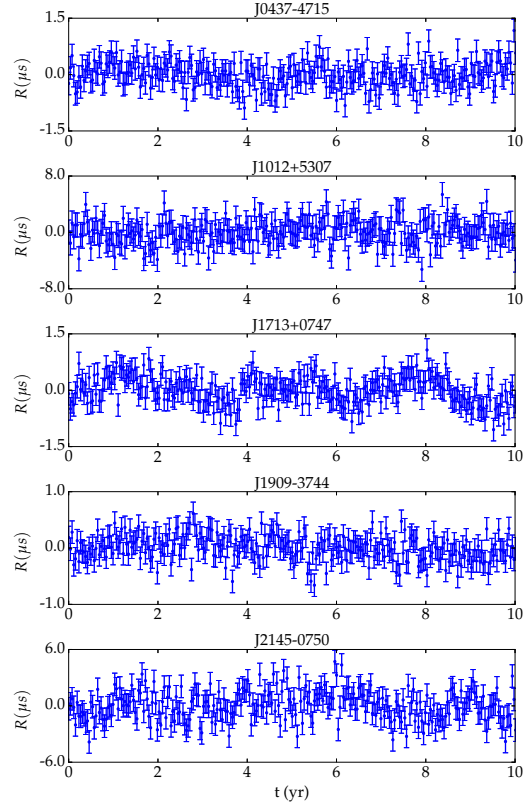
In the following sections, we demonstrate our method by analysing simulated data sets. The sampling of posterior is carried out using the nested-sampling Monte Carlo algorithm MULTINEST (Feroz et al. 2009). A paper where the presented method is applied to the first *International Pulsar Timing Array* data (Verbiest et al. 2016), is now in preparation.

3 DEMONSTRATION AND VERIFICATION

We simulate timing data for five pulsars from the IPTA pulsar list (Verbiest et al. 2016), namely PSRs J0437–4715, J1012+5307, J1713+0747, J1909–3744 and J2145–0750. These pulsars have the lowest level of timing residuals and cover a wide distribution on the sky, so are suitable for our algorithm verification. The parameters of timing noise injected in the simulated data are listed in Table 1, where the timing precisions are from the root-mean-square values of residuals in Verbiest et al. (2016). The properties of the red noise are consistent with the values in Caballero et al. (2016) and Lentati et al. (2016). We simulate the data with a cadence of two weeks and total length of ten years.

We address two scenarios here,

CASE 1 If there are no detectable UMOs, we derive upper limits on their masses.

**Figure 1.** The simulated data in CASE 1. We do not inject the UMO signal in the data, and the structured waveform is due to the red noise of each pulsar.

CASE 2 If the UMO signal is strong, we measure their orbital elements.

We use the following recipe to simulate our data.

(i) Simulate the perfect TOAs for each pulsar using TEMPO2.

(ii) Add the white and red noise according to the noise parameters, where the red noise is synthesised from the given spectrum using the fine frequency grid of $4 \times 10^{-2} \text{ yr}^{-1}$.

(iii) For CASE 2, we inject the UMO induced signal.

Data analysis and results of case 1. In this case, the UMO signal is not injected. We use Bayesian techniques to derive the upper limit for the mass of UMO. The timing residuals of the simulated data set are plotted in Figure 1.

Our data analysis consists of two major steps. In the first step, we quantify if we *detect* the UMO, while in the second step, we perform parameter *inference*. We use Bayes factor (K) to evaluate the detection significance. To do so, we need two Bayesian samplings, one using the model including only the noise parameters and the other one using the model including both noise parameters and UMO parameters. Then the Bayes factor K is the ratio between the Bayesian evidence of the two model. For the data in Figure 1, we get $2 \log K = 0.2$. Based on the interpretation of

Table 2. The seven parameters of UMO in Case 2. The errors here report the 68% confidence level.

Parameter	Simulation	Inference
$\log_{10}(m/M_{\odot})$	-9.3	$-9.33^{+0.04}_{-0.02}$
$\log_{10}(a/\text{AU})$	0.3	$0.303^{+0.002}_{-0.003}$
e	0.3	$0.36^{+0.05}_{-0.09}$
Ω	1	$0.9^{+0.2}_{-0.1}$
ι	1	$0.9^{+0.1}_{-0.1}$
ω	1	$1.3^{+0.2}_{-0.3}$
φ_0	1	$1.3^{+0.2}_{-0.3}$

the Bayes factor by Kass & Raftery (1995), this is an indication that the simpler model without the presence of UMO signals is preferred, and so this allows us with confidence to assume non-detection for this data set and proceed to the next step.

In the second step, we focus on getting the upper limit for the mass of UMOs. It is more informative to know such upper limits as function of the semi-major axis (a). We therefore go through a grid of semi-major-axis values and perform upper-limit inference. For each value of a , we perform posterior sampling for the rest of the orbit and noise parameters. Using a uniform prior on the mass of UMO, we derive its upper limit. An example of the posterior distribution for a search for UMOs at $a \simeq 0.4 \text{ AU}$ is shown in Figure 2. The corresponding upper limits of the UMO mass as a function of the semi-major axis is presented in Figure 3. As one can see, with this simulated data set, any UMO with mass above $\sim 10^{-9} M_{\odot}$ should be excluded within $\sim 5 \text{ AU}$ of the SSB. The spike at 1 AU is caused by fitting for the position of the pulsar. This removes any sinusoidal component with an annual period, while the much smaller spike with a half-year period ($a \simeq 0.6 \text{ AU}$) results from fitting for parallax, which removes only a sinusoidal component in phase with the Earth’s orbit. The reduction in sensitivity for periods longer than 7 years is due to fitting for the pulse period and spin-down rate, as will be discussed in Section 4.

Data analysis and results of case 2. In this case, we inject the signal of a UMO in the simulated data set and demonstrate the method to measure the parameters of UMO. For the UMO signal, the semi-major axis is chosen to be 2 AU. The mass is $5 \times 10^{-10} M_{\odot}$, i.e. at the 3σ upper limit of CASE 1. A moderate value of 0.3 is selected for the eccentricity. While this value is actually larger than any other planets in the Solar system, we choose it to verify the ability of searching for eccentric orbit. The remaining angle parameters are set arbitrarily to be 1 radian. Table 2 lists those parameters. The injected UMO signal and simulated data are in Figure 4.

As in CASE 1, we computed the Bayes factor and found that $2\log K = 3.6$, which, again based on Kass & Raftery (1995), is a clear preference for the model that includes an UMO. The posterior distribution for the parameter inference is shown in Figure 5. As a comparison, we overplot the reconstructed waveforms using the inferred parameters along with the injected signals in Figure 4. From these figures, one can see that for strong signals, the current algorithm produces compatible UMO parameters compared with the injection values.

4 ANALYTICAL RESULTS AND FUTURE PERSPECTIVES

In this section, we derive the analytic formula for the mass upper limit of the UMO. We verify the analytic formula using simulations and then use the analytic results to investigate the capability of future PTA experiments in detecting the UMOs.

4.1 Analytical formula

The Cramér-Rao bound is a well-studied statistical tool (Fisz 1963) to determine the lowest bound on the variances of estimators. It can be regarded as the upper limits for the none detection, or the errorbar when the parameter is measured. Given the likelihood function, Λ , the expected covariance matrix of parameter error is

$$\langle \delta\epsilon_p \delta\epsilon_q \rangle = \left\langle \frac{\partial \ln \Lambda}{\partial \epsilon} \frac{\partial \ln \Lambda}{\partial \epsilon} \right\rangle_{p,q}^{-1}. \quad (24)$$

Here, the model parameters are described by the vector ϵ . They contain both the timing parameters λ and the UMO parameters ξ . For the Gaussian likelihood, i.e. equation (19), the above Cramér-Rao bound can be reduced to (Slepian 1954)

$$\langle \delta\epsilon_p \delta\epsilon_q \rangle = \left(\frac{\partial \Delta \mathbf{R}}{\partial \epsilon} \mathbf{C}^{-1} \frac{\partial \Delta \mathbf{R}}{\partial \epsilon} \right)_{p,q}^{-1}. \quad (25)$$

To proceed, we further simplify the problem by considering only white noise contribution and we assume that (1) the eccentricity of the UMO is small, i.e. $e \ll 1$, and that (2) there are enough data points such that $N \gg 1$. The first assumption helps to get a closed form for the UMO induced signal, $\Delta \mathbf{R}$. Under the second assumption, we can replace the summation of matrix indices in equation (25) with the continuous time integration. We then get,

$$\langle \delta\epsilon_p \delta\epsilon_q \rangle = \left(\frac{N}{\sigma^2 T} \int_0^T \frac{\partial \Delta \mathbf{R}}{\partial \epsilon} \frac{\partial \Delta \mathbf{R}}{\partial \epsilon} dt \right)_{p,q}^{-1}. \quad (26)$$

For the mass of UMO, equation (26) leads to an analytical expression at the two following limits of the semi-major axis:

$$\frac{\delta m}{M_{\odot}} = \begin{cases} \kappa \frac{\sqrt{2}\sigma c}{\sqrt{N}} a^{-1}, & \text{if } a < \frac{(\sqrt{GMT})^{2/3}}{(120\sqrt{7})^{2/9}}; \\ \kappa \frac{120\sqrt{14}\sigma c}{\sqrt{N}(\sqrt{GMT})^3} a^{7/2}, & \text{if } a > \frac{(\sqrt{GMT})^{2/3}}{(120\sqrt{7})^{2/9}}. \end{cases} \quad (27)$$

where σ is the effective root-mean-square level of pulsar noise,

$$\sigma = \left(\sum_{i=1}^{N_{\text{psr}}} \sigma_i^{-2} \right)^{-0.5}. \quad (28)$$

In the above equations, N is the average number of observation epochs per pulsar, T is the average length of observation, and κ is the sky sensitivity. The latter is the geometric correction factor for taking into account the projection of the signal to the pulsar direction, as in equation (2). The sky sensitivity, κ , approaches unity, when the number of pulsars, $N_{\text{psr}} \gg 1$. For limited number of pulsars, κ can be treated as a factor of 2, as we do for the case of five pulsars in our analysis. The sensibility of this approximation can be

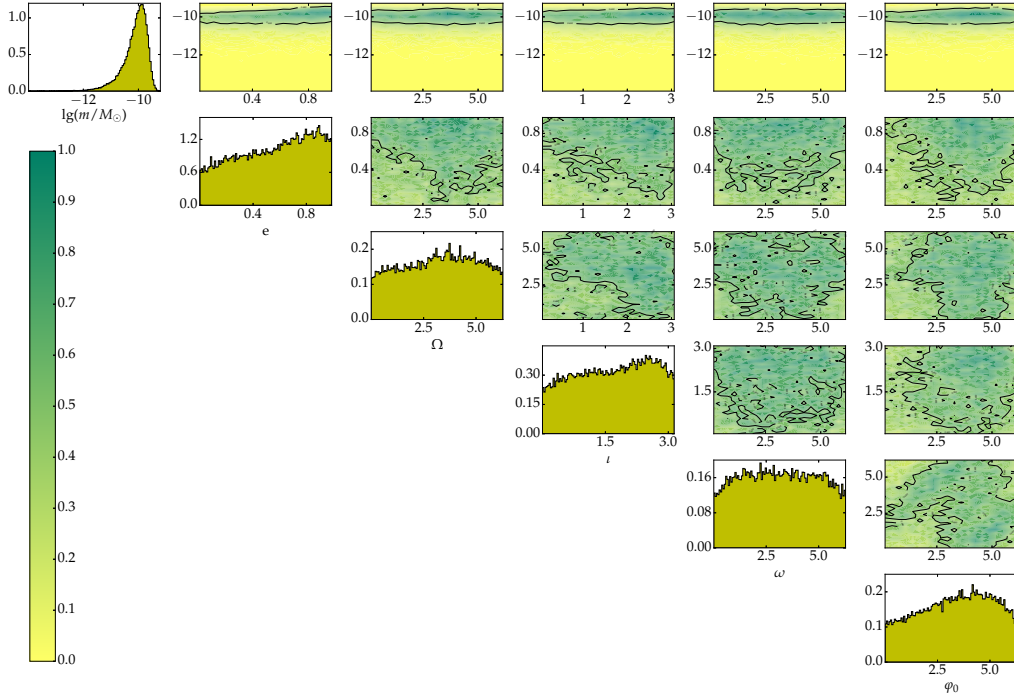


Figure 2. The marginalised posterior distribution of mass m and orbital elements $e, \Omega, i, \omega, \varphi_0$ for the upper-limit analysis at $a \simeq 0.4$ AU of the data set in CASE 1. The diagonal histogram plots are the 1D marginalised posterior distribution of the six parameters. The upper triangular plots show the 2D marginalised posterior, which represent the correlations between parameter pairs. The colour scale indicates the probability density that is rescaled to make the maximum value equal to 1, and the solid contours are the 68% confidence levels. We use the uniform prior to measure the upper limit for the UMO mass, of which the range is from 0 to $10^{-7} M_{\odot}$. The reason of this choice is explained in the main text. The drop of posterior in the low-mass end is due to the choice of prior, and does not indicate a detection of non-zero mass.

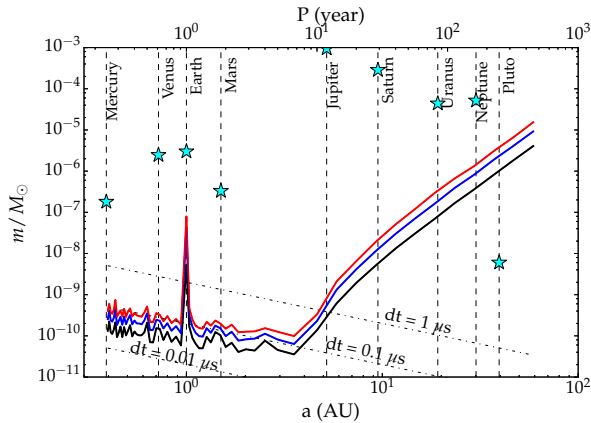


Figure 3. The upper limits for the mass of UMO at different distance to the SSB are shown in solid curves, with confidence levels of 1σ (black), 2σ (blue) and 3σ (red). The vertical dashed lines indicate the semi-major axis of the major planets in the Solar system, and the star marks the corresponding mass. The dot-dashed lines show the expected amplitude ($\frac{ma}{M_{\odot}c}$) of the residuals induced by a mass at given semi-major axis.

illustrated by plotting the value of κ for the five pulsars we used as shown in Figure 6.

In equation (27), there are two cases depending on the value of a . For the case of a small a , the frequency of the UMO signal is high such that the UMO signal and the quadratic pulsar spin-down signal are uncorrelated. The error of UMO mass is inversely proportional to a because of equation (3), and in this regime, the UMO located farther to the SSB is easier to detect. In the second regime, when a becomes larger, the data span is not long enough to cover several orbital periods, so the short-duration sinusoidal function is correlated with the quadratic pulsar spin-down signal. The UMO signal is no longer periodic in the data. The $a^{7/2}$ dependence comes from the cubic function left in the residuals due to the fitting of pulsar period and period derivative.

To assess the predictive power of equation (27), we employ it to calculate analytically the UMO-mass sensitivity curves for the CASE 1 simulations and compare it with the results from the Bayesian analysis. The results are shown in Figure 7. One can see that such an analytical expression, although much simplified, still encapsulates the major features of the sensitivity curve. The deviations between the analytical expression and the numerical results become significant, when a is large. In this regime, the UMO orbital period is

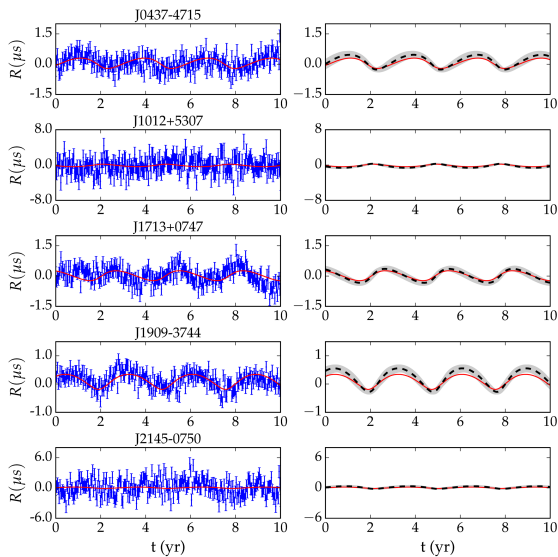


Figure 4. The simulated data, the injected and the recovered waveforms in Case 2 for the five pulsars. The left column shows the timing residuals and the injected waveform of UMO (the solid line with no errorbar). The recovered waveforms are plotted in black dashed curves in the right column, and the grey stripes indicate the 68% confidence regions. The solid curves are the injections, plotted for comparison.

larger than the data length, and the estimations of mass upper limit become highly affected by the choice of prior and red noise modelling. The analytical expression gives the correct power index, i.e. $\delta m \propto a^{7/2}$, but the numerical factor becomes less reliable.

The Cramér-Rao bound will fail for the situation, when a unique un-biased estimator is not available (Lee et al. 2011). For the current UMO problem, this happens, when the number of pulsars is limited. In certain cases, a limited number of pulsars have much better precision than the rest of pulsars in the timing array. This effectively reduces the number of pulsars contributing to the analysis. We show an ill-conditioned example in Figure 8, and the corresponding posterior distributions from the Bayesian analysis in Figure 9. Although the recovered waveform is very different for PSR J2145–0750, the timing precision limits us from differentiating the two sets of parameters. In general, three parameters can be measured from the signal of one pulsar, namely the amplitude, frequency and phase. We will need more than three pulsars to measure the seven parameters describing the UMO.

4.2 Prediction

In the near future, discoveries of more stable millisecond pulsars and new commissions of advanced instruments will continuously increase the quality of pulsar-timing data. The *Five-hundred-meter Aperture Spherical radio Telescope* (FAST; Nan et al. 2011), the *QiTai 110m radio Telescope* (QTT; Wang 2017) and the *Square Kilometre Array* (SKA; Kramer & Stappers 2010), will significantly improve the tim-

ing precision for a large number of pulsars. We expect the upper limit for the UMO mass will be more stringent.

We estimate the future upper limits of the UMO mass using equation (27), and the results are summarized in Figure 10. One can see that with 10-year pulsar timing for 20 pulsars to the precision of 100 ns, we can push the mass upper limits to 10^{-11} to $10^{-12} M_{\odot}$, i.e. 10^{-8} to 10^{-9} Jupiter mass. Other cases show the improvement of upper limits with longer data span, more pulsars and increased precision. The upper limits can be an order of magnitude better, if we use 20-year data of 20 pulsars with a precision of 30 ns. Since the timing precision of 30 ns over 20 years is unlikely due to noise processes in pulsars, the result will probably look that good only for UMOs with periods of ~ 5 years. The upper limit is also the precision of measurements, so we expect that future PTAs will measure the mass of Jovian system with a fractional precision of 10^{-8} to 10^{-9} , which is comparable to the existing IAU uncertainties (Luzum et al. 2011).

5 DISCUSSIONS AND CONCLUSIONS

We have developed a method to search for UMOs in the Solar system using PTA data. Our algorithm is based on the Bayesian data-analysis framework, where the detection significance is evaluated using Bayes factor and the parameter inference is performed using posterior sampling. We have verified the method using simulated data sets. The current method is capable of producing the upper limit for the mass of UMOs and to measure the orbit elements. As we have demonstrated, the parameter inference matches the injection values in the simulation. We have also derived the analytical expression for the upper limits of UMO mass. The upper limits using the Bayesian inference agree well with our analytical expression. With this method, we have estimated the future perspectives of detecting the UMOs using pulsar timing array. The method has different selection effects compared to the traditional planet detections, e.g. optical surveys, that even the invisible exotic objects can be detected, as long as they are massive.

Champion et al. (2010) measured the mass error of the known planets, based on the Solar system ephemeris DE421. By employing a dynamical model for the orbit, our method measures the properties of UMOs, both the mass and orbital elements. The Bayesian framework helps to simultaneously analyze the signal of UMOs, pulsar timing model in the presence of other noise processes. We have assumed Keplerian orbits for the UMOs and neglected all perturbations. Here, the assumption saves us from implementing the full dynamic modelling of Solar system as in Seidelmann (2005). In our model, we neglect all propagation effects of pulsar signal due to the UMO other than Rømer delay. The higher order terms, e.g. Shapiro delay and gravitational red shift of UMO, will be not be measurable for objects much lighter than the Jupiter. While obviously having the advantage of fully exploring the orbital parameters, the method is currently practically limited to study light objects not in orbit with other planets. Nevertheless, the algorithm presented can serve as a basis on which we can found attempts to perform full dynamical modelling in the future. It is noteworthy that inaccuracies in the used Solar system ephemeris,

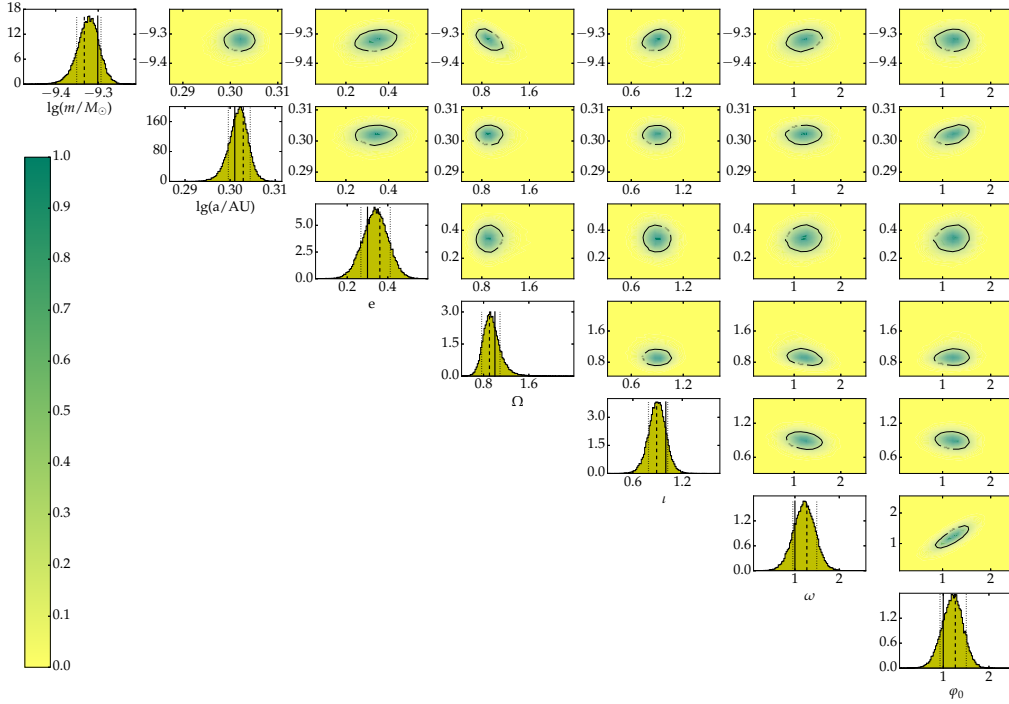


Figure 5. The marginalised posterior probability distribution of mass m and orbital elements $a, e, \Omega, \iota, \omega, \varphi_0$ in Case 2. In the diagonal 1D marginalised posteriors, the solid vertical lines indicate the injected value of parameters, and the dashed lines represent the maximum likelihood estimation with the 68% confidence level marked by the dotted lines. Similar to Figure 2, the upper triangular panels are the 2D marginalised posterior distributions.

are identified as one of the main sources of correlated noise in PTA data that impede efforts for direct nHz GW detections (e.g. Tiburzi et al. 2016; Taylor et al. 2017; Wang et al. 2017). Modelling approaches such as the one presented in this work, can help in efforts to mitigate this noise and improve the PTA sensitivity to GWs (Lentati et al. 2015; Li et al. 2016). We also note, that while discoveries of previously unknown bodies in the solar system with PTA blind searches may be difficult, the use of more evolved dynamical models may allow in the future PTAs to contribute in imposing meaningful constraints on the parameter space of independently proposed unknown planets (e.g. Batygin & Brown 2016; Brown & Batygin 2016), as shown in Figure 10.

Both the pulse period P and period derivative \dot{P} are fitted in the timing model, which absorbs the linear and quadratic signals. In this way, our method is not sensitive to the acceleration of the Solar system, and it searches for the ‘jerk’ in the timing signal for long-period planets, i.e. we search for the time *derivative* of Solar system acceleration for the second case in equation (27). There are works to constrain the Solar system acceleration directly. Zakamska & Tremaine (2005) proposed to detect the Solar system acceleration using \dot{P} distribution of millisecond pulsars (under the assumption of position-independent distribution) or orbital period derivative of binary pulsars. Verbiest et al. (2008) and Deller et al. (2008) timed the binary PSR

J0437–4715 and determined the upper limit of Solar system acceleration using orbital period derivative.

Our analytical expression for the mass upper limit is derived using Cramér-Rao bound. Since it theoretically predicts the best possible upper limit for any unbiased estimator, it is a very useful tool to cross check the data-analysis as well as to make predictions to help planning future observations. As we see, timing 20 pulsars to the precision of 100 ns, will rule out any unknown objects with mass of 10^{-11} to $10^{-12}M_{\odot}$ within 10 AU around the Sun. For dark matter clumps, this will be a factor of 10^2 better than the current limit (Pitjev & Pitjeva 2013; Pitjeva & Pitjev 2013). The PTAs become sensitive tools to study the Solar system mass distribution and dynamics. We expect that advanced instruments (e.g. FAST, SKA, and QTT) in the future will benefit the field.

ACKNOWLEDGMENTS

This work was supported by XDB23010200, National Basic Research Program of China, 973 Program, 2015CB857101 and NSFC U15311243, 11690024, 11373011. We are also supported by the MPG funding for the Max-Planck Partner Group. The computation was performed using the cluster DIRAC in KIAA and the TIANHE II supercomputer at Guangzhou supported by Special Program for Applied

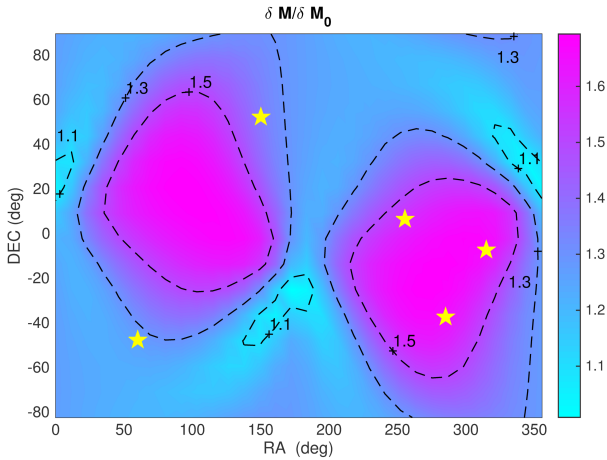


Figure 6. The geometric correction factor κ for the five pulsars we used. The yellow pentagons are the five pulsars. The colour scale together with the contours indicates the value of κ . Here we plot κ as a function of right ascension (RA) and declination (Dec.) of the orbit pole, i.e. the projection direction of the orbital angular momentum on the celestial sphere. We see that κ becomes larger, when the orbital pole is located around clusters of pulsars. This means that the sensitivity to UMOs drops, when the orbital plane is perpendicular to the pulsar direction.

Research on Super Computation of the NSFC-Guangdong Joint Fund (the second phase) under Grant No.U1501501. We thank Joris Verbiest, William Coles and Stephen Taylor for helpful comments.

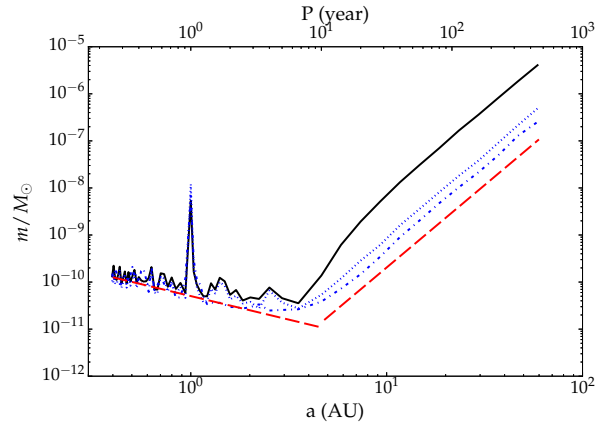


Figure 7. The analytical upper limits for the mass of UMO. The red dashed lines show the approximations in the limits of $T \gg a^{1.5}$ and $T \ll a^{1.5}$ as in equation (27). The 68% upper limit in Fig. 3 is plotted in a black solid curve for comparison. The blue dotted line is the upper limit when the eccentricity prior is confined to $0 \leq e < 0.1$. The blue dot-dashed line is the upper limit when we do not fit for red noise parameters.

REFERENCES

- Batygin K., Brown M. E., 2016, *AJ*, 151, 22
 Blanco-Pillado J. J., Olum K. D., Shlaer B., 2014, *Phys. Rev. D.*, 89, 023512
 Brown M. E., Batygin K., 2016, *ApJ*, 824, L23
 Caballero R. N., et al., 2016, *MNRAS*, 457, 4421
 Champion D. J., Hobbs G. B., Manchester R. N., et al., 2010, *ApJL*, 720, L201
 Cordes J. M., 2013, *Classical and Quantum Gravity*, 30, 224002
 Deller A. T., Verbiest J. P. W., Tingay S. J., Bailes M., 2008, *ApJ*, 685, L67
 Edwards R. T., Hobbs G. B., Manchester R. N., 2006, *MNRAS*, 372, 1549
 Feroz F., Hobson M. P., Bridges M., 2009, *MNRAS*, 398, 1601
 Fisz M., 1963, *Probability Theory and Mathematical Statistics*. New Yorker: Wiley
 Folkner W. M., Williams J. G., Boggs D. H., 2009, *Interplanetary Network Progress Report*, 178, 1
 Foster R. S., Backer D. C., 1990, *ApJ*, 361, 300
 Gregory P. C., 2005, *Bayesian Logical Data Analysis for the Physical Sciences: A Comparative Approach with ‘Mathematica’ Support*. Cambridge University Press
 Hellings R. W., Downs G. S., 1983, *ApJL*, 265, L39
 Hobbs G., Coles W., Manchester R. N., et al., 2012, *MNRAS*, 427, 2780
 Hobbs G. B., Edwards R. T., Manchester R. N., 2006, *MNRAS*, 369, 655
 Hotan A. W., van Straten W., Manchester R. N., 2004, *PASA*, 21, 302
 Kass R. E., Raftery A. E., 1995, *Journal of the american statistical association*, 90, 773
 Kramer M., Stappers B., 2010, in *ISKAF2010 Science Meeting - ISKAF2010, June 10-14, 2010 Assen, the Netherlands LOFAR, LEAP and beyond: Using next generation telescopes for pulsar astrophysics*. p. 10
 Lee K. J., Bassa C. G., Janssen G. H., Karuppusamy

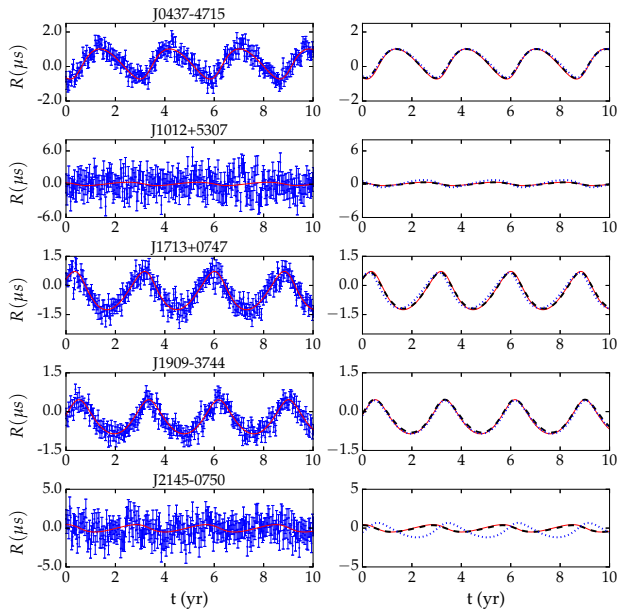


Figure 8. The simulated data and recovered waveform of an ill-conditioned example. The left column shows the timing residuals and the simulated waveform of UMO (red solid line). The waveform recovered from the two different sets of parameters are plotted in dashed black and dotted blue lines in the right column. As one can see, when the number of pulsars with good signal-to-noise ratio is limited, multiple solutions will be allowed.

R., Kramer M., Liu K., Perrodin D., Smits R., Stappers B. W., van Haasteren R., Lentati L., 2014, *MNRAS*, 441, 2831

Lee K. J., Wex N., Kramer M., Stappers B. W., Bassa C. G., Janssen G. H., Karuppusamy R., Smits R., 2011, *MNRAS*, 414, 3251

Lentati L., Shannon R. M., Coles W. A., et al., 2016, *MNRAS*, 458, 2161

Lentati L., Taylor S. R., Mingarelli C. M. F., et al., 2015, *MNRAS*, 453, 2576

Li L., Guo L., Wang G.-L., 2016, *Research in Astronomy and Astrophysics*, 16, 58

Loeb A., Zaldarriaga M., 2005, *Phys. Rev. D.*, 71, 103520

Lorimer D., Kramer M., 2005, *Handbook of Pulsar Astronomy*. Cambridge Univ. Press, Cambridge, UK

Luzum B., Capitaine N., Fienga A., Folkner W., Fukushima T., Hilton J., Hohenkerk C., Krasinsky G., Petit G., Pitjeva E., Soffel M., Wallace P., 2011, *Celestial Mechanics and Dynamical Astronomy*, 110, 293

Manchester R. N., Taylor J. H., 1977, *Pulsars..* W. H. Freeman, San Francisco, CA, USA

Nan R., Li D., Jin C., Wang Q., Zhu L., Zhu W., Zhang H., Yue Y., Qian L., 2011, *International Journal of Modern Physics D*, 20, 989

Pitjev N. P., Pitjeva E. V., 2013, *Astronomy Letters*, 39, 141

Pitjeva E. V., Pitjev N. P., 2013, *MNRAS*, 432, 3431

Seidelmann P. K., 2005, *Explanatory Supplement to the Astronomical Almanac, Revised Edition*. University Sci-

ence Books, Mill Valley, CA

Sheppard S. S., Trujillo C., 2016, *AJ*, 152, 221

Slepian D., 1954, *Transactions of the IRE Professional Group on Information Theory*, 3, 68

Standish E. M., 1998, *JPL IOM*, 312, F-98-408, 312, F

Taylor S. R., Lentati L., Babak S., Brem P., Gair J. R., Sesana A., Vecchio A., 2017, *Physical Review D*, 95, 042002

Tiburzi C., Hobbs G., Kerr M., Coles W. A., Dai S., Manchester R. N., Possenti A., Shannon R. M., You X. P., 2016, *MNRAS*, 455, 4339

van Haasteren R., Levin Y., McDonald P., Lu T., 2009, *MNRAS*, 395, 1005

Verbiest J. P. W., Bailes M., van Straten W., Hobbs G. B., Edwards R. T., Manchester R. N., Bhat N. D. R., Sarkissian J. M., Jacoby B. A., Kulkarni S. R., 2008, *ApJ*, 679, 675

Verbiest J. P. W., Lentati L., Hobbs G., et al., 2016, *MNRAS*, 458, 1267

Wang J. B., Coles W. A., Hobbs G., et al., 2017, *MNRAS*, 469, 425

Wang N., 2017, *Scientia Sinica Physica, Mechanica & Astronomica*, 47, 059501

Wu F., Xu R.-X., Ma B.-Q., 2007, *Journal of Physics G Nuclear Physics*, 34, 597

Zakamska N. L., Tremaine S., 2005, *AJ*, 130, 1939

This paper has been typeset from a $\text{\TeX}/\text{\LaTeX}$ file prepared by the author.

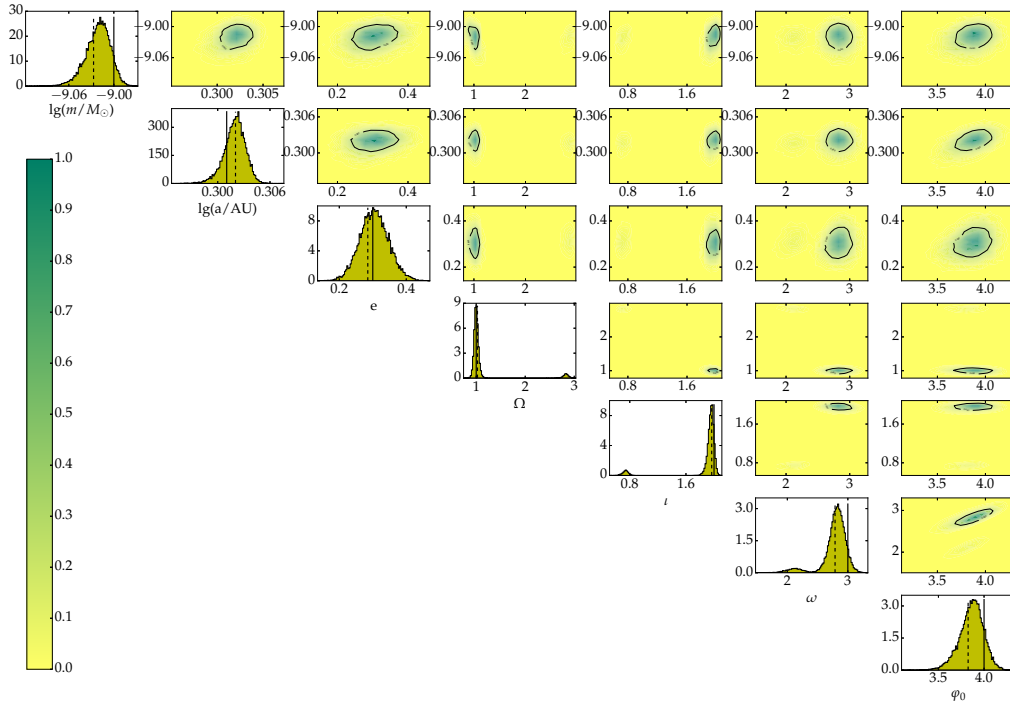


Figure 9. The same as Figs 2 and 5, but for an ill-conditioned simulation. The two peaks in the posterior of Ω , l and ω indicate the multiple solutions.

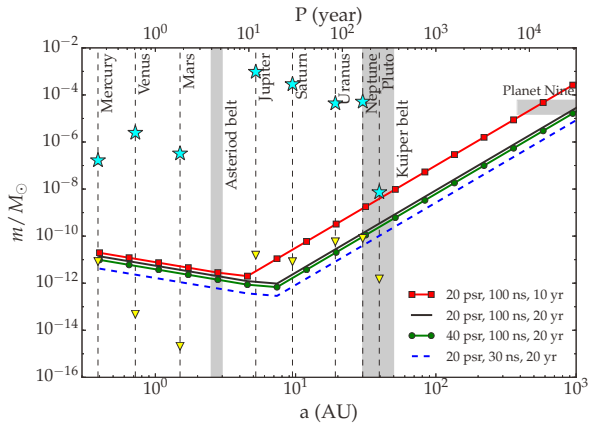


Figure 10. The predicted upper limits for the mass of UMO in four cases, with different combinations of the number of pulsars, timing precision and data span. For all cases, the cadence of observation is chosen to be two weeks. The vertical dashed lines indicate the semi-major axis of the major planets in the Solar system, and the star marks the corresponding mass. The official IAU uncertainties on the planetary masses are plotted as triangles for comparison (Luzum et al. 2011). The mass at 1 AU will be practically unconstrained because of fitting pulsar position, so the parameters of Earth are not plotted. The grey regions show the positions of the asteroid belt, Kuiper belt and the parameter space of Planet Nine (Brown & Batygin 2016). Note that the prediction is for circular orbit, and the upper limit will be larger for an eccentric orbit.